Beam Seas Tests of Two Different Ship Models in Large Amplitude Regular Waves

Angelo Olivieri, *INSEAN (Italian ship model basin), Via di Vallerano 139, 00128 Roma, Italy*

Emilio F. Campana, *INSEAN (Italian ship model basin), Via di Vallerano 139, 00128 Roma, Italy*

Alberto Francescutto, *University of Trieste, Trieste, Italy*

Fred Stern, *IIHR Hydroscience & Engineering, The University of Iowa, Iowa City, IA, 52242, USA*

ABSTRACT

The purpose of the paper is the study of the extreme ship motions through properly designed experiments aimed at both fundamental physical understanding and at collecting high-quality data for CFD codes validation. Two different ship models have been tested in regular beam waves to obtain repeatable data for time histories of measured motions, forces and moments. The tested models are geosyms of the DTMB model 5415 (INSEAN model 2385) and of the ONR Tumblehome (INSEAN model 2498), which are preliminary designs of surface combatants ca. 1980 and present time. The same scale has been adopted for both models ($\lambda = 46.6$). Models have been both equipped with bilge keels. The adopted test conditions are free heave and roll, whereas the other degrees of freedom are constrained. Forces and moments have been acquired for the restrained motions. Two series of five repeated tests have been carried out, with medium and large wave amplitudes at the resonant frequency for both models. The precision limit (PI) for all variables has been evaluated.

Keywords: *semicaptive tests, repeated tests, certified experimental data.*

1. INTRODUCTION

The problem of the certification of the safety of a ship is nowadays the more important aim to be achieved in the ship design. The prediction of the unsafe conditions for a ship in rough seas is still committed to hydrostatic calculations and the stability criteria present lack of clarity and sometimes logic in regulation systems throughout the world (Rojas and Belenky, 2003).

More recent works on capsizing have been conducted mainly on fishing vessels, cargo and container ships using potential hydrodynamics with the development of nonlinear seakeeping simulation codes such as, FREDYN, DINMA, SIMBEL, MD2004 (24th ITTC , 2005). Nevertheless, the adopted mathematical models for the capsizing description vary very much between different research groups and the prediction of extreme motions just in few cases and only qualitatively matches the experimental results. Moreover, the mathematical models for capsizing involve a number of factors without clear guidance in place on which of these should be taken into account.

At present, there is still a lack in the understanding of physical phenomena involved in capsizing and, even more important, there is a regulation system that is often not clear in settling universal stability criteria.

On the experimental side, the free running tests reproduce, at least qualitatively, the real scenario, but the obtained results are affected by many factors and often they are not repeatable. Oppositely, the captive tests can give repeatable and certifiable experimental results, but they provide information only for forces and moments, being all the ship motions restrained.

The recent improvements of the unsteady RANS codes for the pitch and heave and for the roll motion predictions (Wilson, Carrica and Stern, 2006) allow us to nominate these solvers as good candidates in order to approach the ships capsizing problem, but for this purpose, they have to be validated by comparison with experimental results obtained by properly designed experiments.

As underlined, the free running tests cannot be used to build a database of certified experimental results provided with uncertainty assessment, whereas the captive tests do not give information on the ship motions. Hence, properly designed experiments have to be performed in order to give reliable information for testing the numerical codes.

Objective of the present work is to perform a series of repeatable experiments in semicaptive conditions (2 DoF) in order to collect an experimental database to be used as benchmark for unsteady RANS codes or other numerical solvers. The semicaptive conditions have been chosen in order to obtain repeatable tests and, at the same time, verify the capability of the numerical solvers in predicting large amplitude motions. Furthermore, the tests have been carried out for two different hull forms, which are geosyms of the DTMB model 5415 (INSEAN model 2385) and of the ONR Tumblehome (INSEAN model 2498) and the results have been compared, showing interesting differences between them.

The tests have been performed in the same conditions and the model scales are the same ($\lambda_{2385} = \lambda_{2498} = 46.6$). The tests have been done in regular large amplitude beam waves. The allowed motions are roll and heave, while for the constrained DoF, forces and moments have been acquired. The results presented here represent a part of a wider project sponsored by ONR. The whole project includes head seas and following seas test, which are currently in progress.

2. MODELS AND TESTS DESCRIPTION

The two tested hull forms are geosyms of the DTMB model 5415 (INSEAN model 2385) and of the ONR Tumblehome (INSEAN model 2498). The two models are in the same scale ($\lambda = \lambda_{2385} = \lambda_{2498} = 46.6$) and are both equipped with bilge keels. They have been tested in the INSEAN basin n. 2 (220 m long, 9 m wide and 3.5 m deep), which is equipped whit a flap wave maker at the basin end. The tests on the two models have been carried out using the same experimental apparatus. Beam seas tests have been performed at the resonant frequency, which has been determined exciting the models with small amplitude waves. During the tests the models have been disposed normally to the generated wave front, in the center of the basin in length and width. The models were free to roll and heave, with the other DoF restrained. For the restrained motions the forces and moments at the constraint have been measured. Three different wave slopes have been adopted, corresponding to small amplitude ($ak \approx 0.035$), medium amplitude ($ak = 0.073$) and large amplitude waves ($ak = 0.156$), in order to evaluate the rising and development of the nonlinearities in the allowed motions and in the measured forces and moments. The wave height has been measured by a servomechanic probe (Kenek SH) mounted 1 model length upstream the tested model. The lines of the two tested models are shown in figures 1 and 2, while the main model parameters are given in tables 1 and 2. The bilge keels profiles and locations are shown in figures 3, 4 and 5. The DTMB model 5415 (INSEAN 2385, fig. 6) is 3.048 m long, while the ONR Tumblehome (INSEAN 2498, fig. 7) is 3.305 m (L_{PP}).

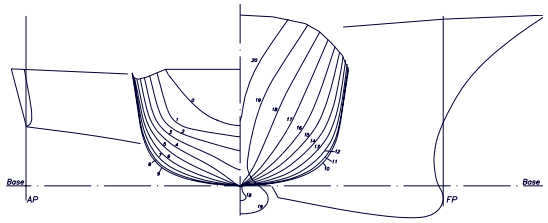

Figure 1: DTMB 5415 lines, bow and stern profiles

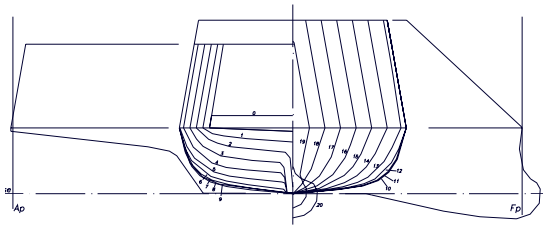

Figure 2: ONR Tumblehome lines, bow and stern profiles

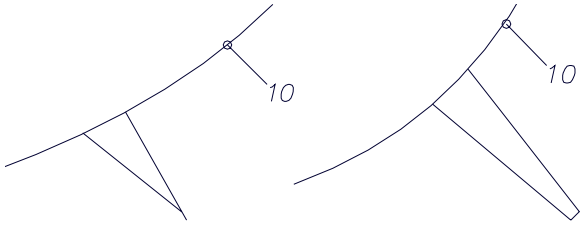

Figure 3: DTMB 5415 (left) and ONR Tumblehome (right) bilge keels profiles at midship

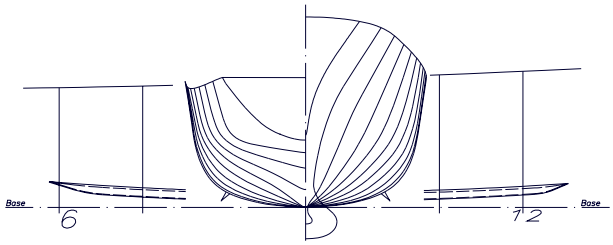

Figure 4: DTMB 5415 bilge keels: longitudinal extent and position

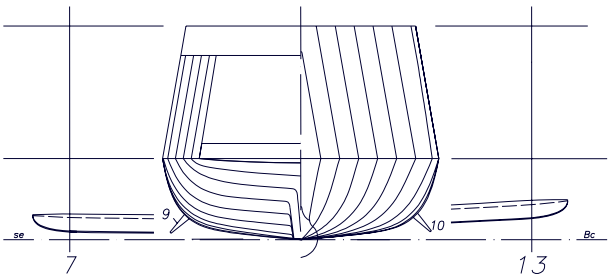

Figure 5: ONR Tumblehome bilge keels: longitudinal extent and position

The heave and roll motions have been measured by means of optical motion tracker (Krypton), while the sway and surge forces have been measured by load cells which have been lodged inside a joint (figure 8) fixed to the model in correspondence of the center of gravity (CG). The pitch moment has been measured by a load cell mounted 100 mm upstream the CG, while the yaw moment has been measured by a torque cell. The torque cell connects the joint to a vertical bar, which is free to slide into a cylindrical guide fixed to the carriage. The yaw motion is inhibited by an additional guide that moves parallel to the vertical bar and rigidly fixed to it. The additional guide is mounted with 200 mm arm with respect to a vertical line passing through the CG. The same set of load cells and the same torque cell have been used for both models.

Table 1: main parameters of the DTMB 5415 (INSEAN model 2385)

DTMB 5415 (λ = 46.6)	
L_{PP}	3.048 m
Draft (T)	0.132 m
Beam (B_{WL})	0.406 m
Displ. (V)	0.083 m^3
LC_G	1.550 m (Aft of FP)
KG	0.162 m
GM_T	0.044 m
K_{XX}	0.162 m (40% B_{WL})
$K_{YY} = K_{ZZ}$	0.762 m (25% L_{PP})
Bilge Keels	c = 19.55 mm L = 1015 mm

Table 2: main parameters of the ONR Tumblehome (INSEAN model 2498)

ONR Tumblehome (λ = 46.6)	
L_{PP}	3.305 m
Draft (T)	0.118 m
Beam (B_{WL})	0.403 m
Displ. (V)	0.087 m^3
LC_G	1.708 m (Aft of FP)
KG	0.165 m
GM_T	0.043 m
K_{XX}	0.153 m (38% B_{WL})
$K_{YY} = K_{ZZ}$	0.826 m (25% L_{PP})
Bilge Keels	c = 33.55 mm L = 1098 mm

Figure 6: INSEAN model 2385, geosym of the DTMB 5415

Figure 7: INSEAN model 2498, geosym of the ONR Tumblehome

The smallest adopted wave slope was $ak = 0.036$ for the 2385 and $ak = 0.034$ for the 2498, while the medium and the highest wave slopes were $ak = 0.073$ and $ak = 0.156$ for both models. The medium and high wave slope tests have been repeated five times and the precision limit has been determined.

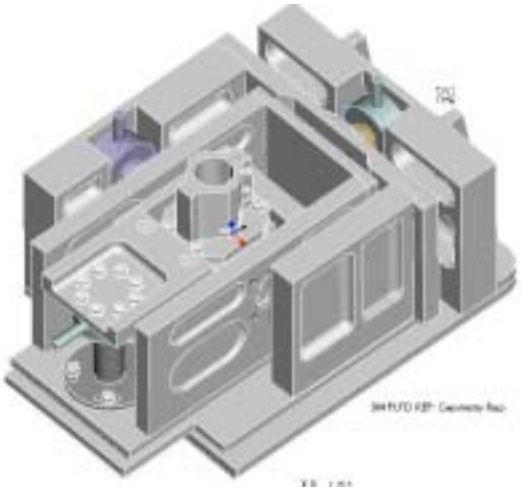

Figure 8: Illustration of the joint; the torque cell has been mounted on the top.

3. RESULTS

As a first step, the resonant frequency for small amplitude waves has been determined for both models, exciting them by a series of regular wavetrains with different frequencies. The obtained resonant frequency for the 2385 is $f_{2385} = 0.675$ Hz, while for the 2498 is $f_{2498} = 0.650$ Hz. Curiously, for both models this corresponds to a ratio between wavelength of the exciting waves and model length $\lambda/L_{PP} = 1.12$.

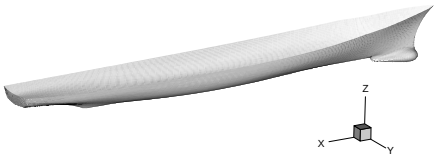

Figure 9: DTMB 5415 coordinate system with origin on the center of gravity; the same coordinates are used for the ONR Tumblehome

From every set of five repeated tests the phase locked average has been determined for all the measured variables. The results are presented in terms of averaged time histories, Fourier transform, combined plots and phase diagrams. The amplitude of the motions and forces and moment, determined as half a difference between minimum and maximum has been plotted as function of the wave slope.

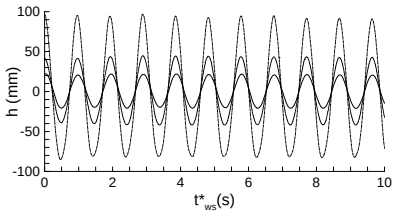

Figure 10: Wave height time histories for the three cases analyzed for the DTMB 5415; the time is normalized by the resonant frequency f = 0.675 Hz

Figure 9 shows the adopted coordinate system, which has the origin at the center of gravity for both models. In figure 10 the wave height time histories for the three adopted wave slopes are shown for the DTMB 5415.

In the present paper, only the main points of the experimental campaign are described, while the complete set of figures with time histories, Fourier analysis, combined plots and phase diagrams of all variables is shown in (Olivieri, Campana, Francescutto and Stern, 2006).

3.1 DTMB model 5415 results (INSEAN model 2385)

The heave motion follows almost perfectly the wave height for all three cases and the roll motion shows no evidence of nonlinearities

(figures 11 and 12). In figure 13 the heave amplitude $||Z_G||$ is shown as a function of the wave height amplitude ||h|| together with the roll amplitude $||\phi°||$ versus the nominal wave slope *ak* . For a general variable *x*:

$$\|x\| = \frac{x_{max} - x_{min}}{2} \quad (1)$$

The heave amplitude is proportional to the wave height, while the roll motion saturates for the highest wave slope.

Nonlinear behavior is shown by the axial force R_X and pitch moment M_Y, whereas the yaw moment M_Z shows no evidence of nonlinearities. The side force R_Y manifests a peculiar shape of the time history, but does not show any evidence of nonlinearities as confirmed by the Fourier analysis (figure 21).

The time histories for R_X, R_Y and M_Y for the three cases are shown in figures 14, 15 and 16 respectively.

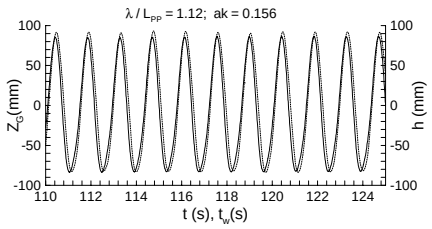

Figure 11: Heave motion (solid line) and wave height (dashed line) time histories for the DTMB 5415, *ak* = 0.156; the wave height is shifted in time the using the linear approximation for the wave celerity.

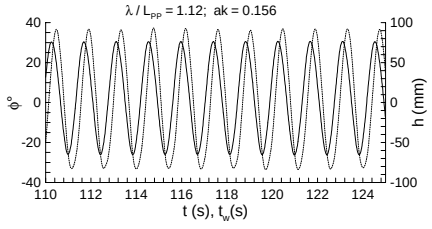

Figure 12: Roll motion (solid line) and wave height (dashed line) time histories for the DTMB 5415, *ak* = 0.156; the wave height is shifted in time the using the linear approximation for the wave celerity.

The period of the R_X time history is 1/4 of the wave period even for small amplitude waves, while the time history of the side force R_Y presents a complex shape without a presence of 2nd or higher harmonics. The pitch moment time histories show the rising of the second harmonic for all three cases.

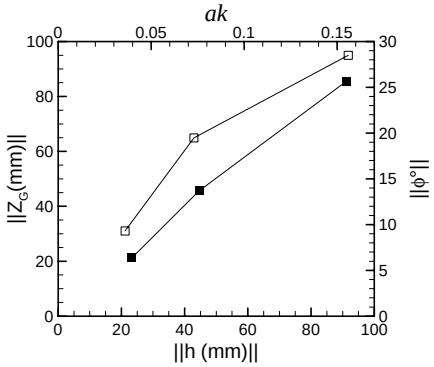

Figure 13: Heave amplitude $||Z_G||$ vs. wave height amplitude ||h|| (filled symbols) and roll amplitude $||\phi°||$ (open symbols) vs. the nominal wave slope *ak*.

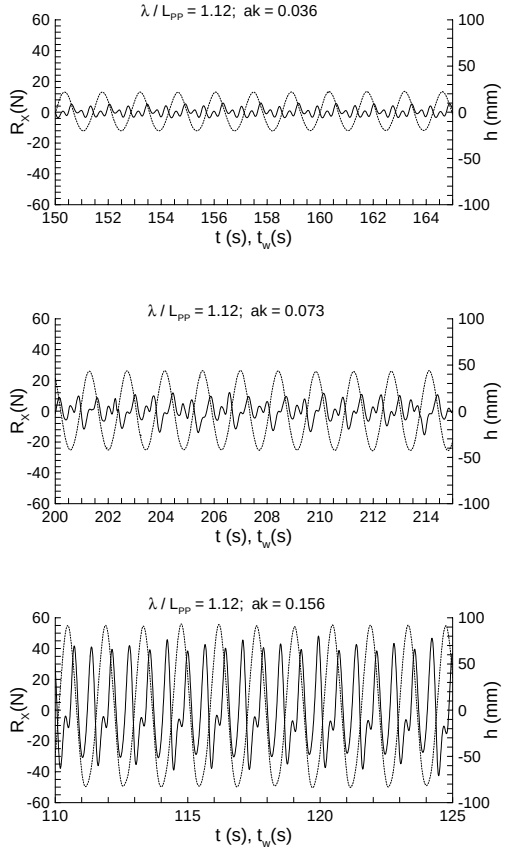

Figure 14: Time histories of the axial force R_X for small, medium and large amplitude waves (solid lines) superimposed to the time histories of the wave elevation (dashed lines)

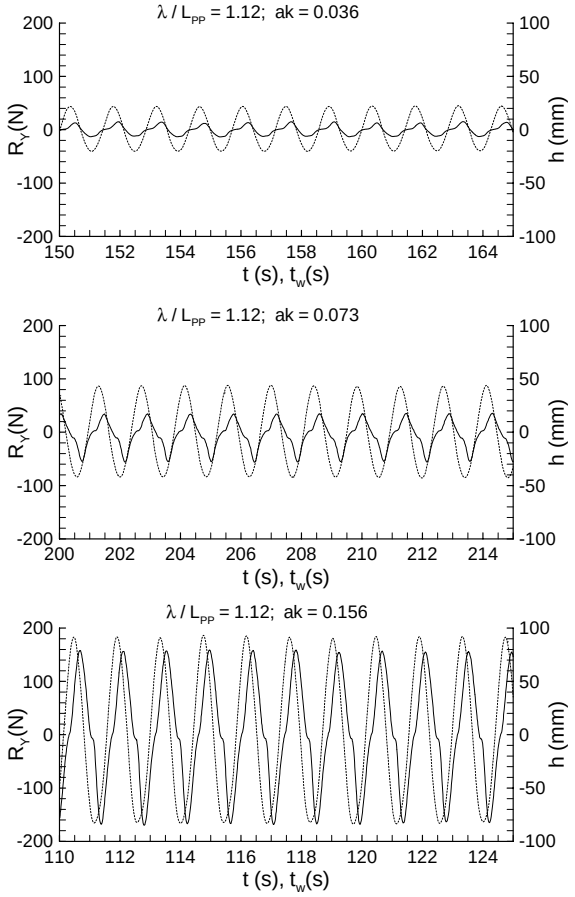

Figure 15: Time histories of the side force R_Y for small, medium and large amplitude waves (solid lines) superimposed to the time histories of the wave elevation (dashed lines)

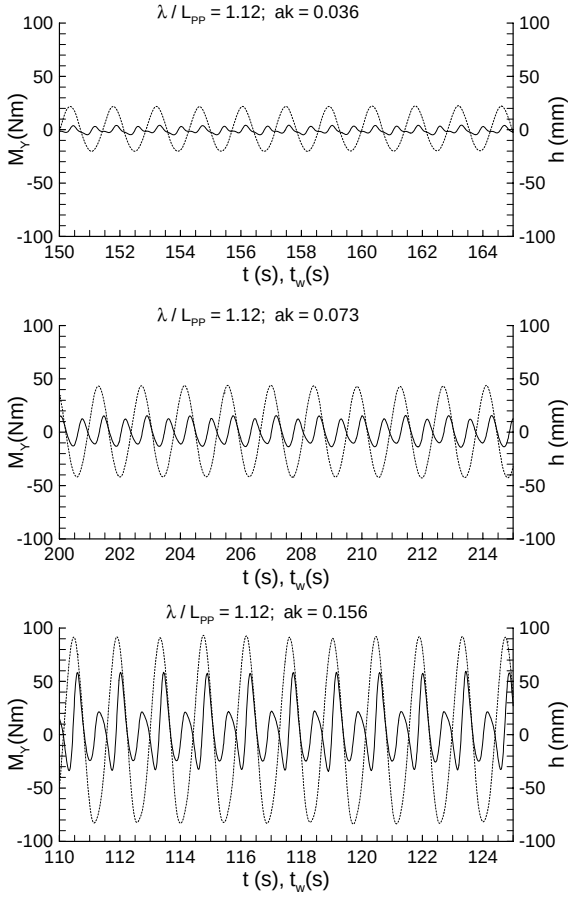

Figure 16: Time histories of the pitch moment M_Y for small, medium and large amplitude waves (solid lines) superimposed to the time histories of the wave elevation (dashed lines)

The amplitude functions of the wave height and heave motion show the presence of a very small superharmonic (figures 17 and 18), while the roll motion does not show any presence of superharmonics (figure 19). The amplitude function of the axial force is shown in figure 20 for all three wave slopes. It is noticeable that for the small wave slope the fourth harmonic dominates, while increasing the wave amplitude the second harmonic becomes leading. The side force and the pitch moment show the same trends of the amplitude function for all tested wave slopes; the results related to $ak = 0.156$ are reported in figures 21 and 22. It is evident that the side force is dominated by the fundamental frequency ($f_{2385} = 0.675$ Hz), while the pitch moment is dominated by the 2nd harmonic, although the fundamental and the 3rd harmonic are not negligible.

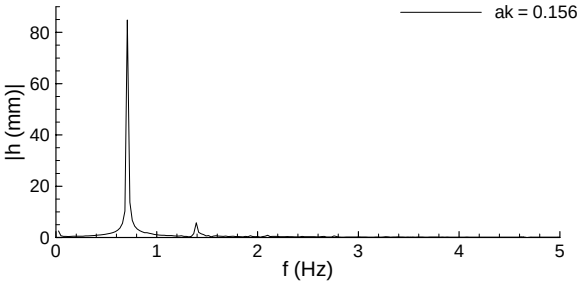

Figure 17: Amplitude function of the wave height h ($ak = 0.156$).

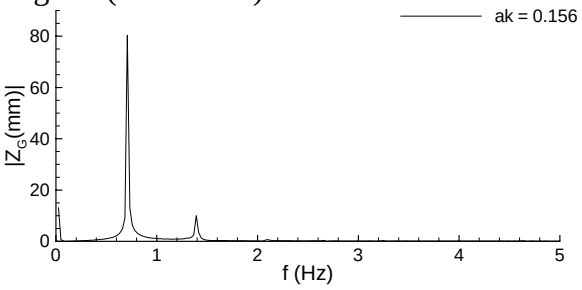

Figure 18: Amplitude function of the heave motion ZG (ak = 0.156).

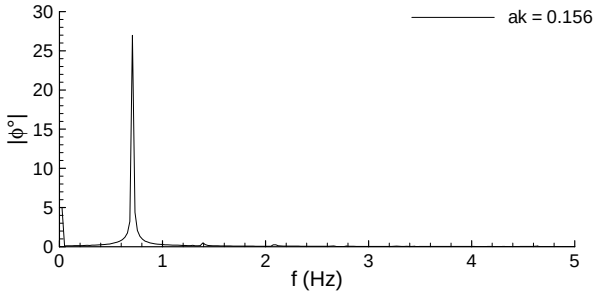

Figure 19: Amplitude function of the roll motion ϕ (ak = 0.156).

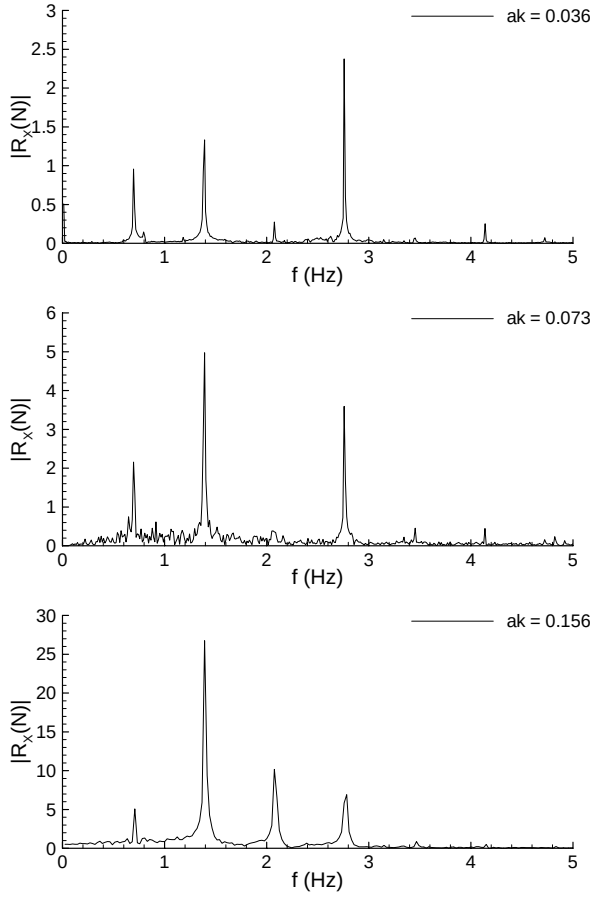

Figure 20: Amplitude function of the axial force RX for small, medium and large amplitude waves.

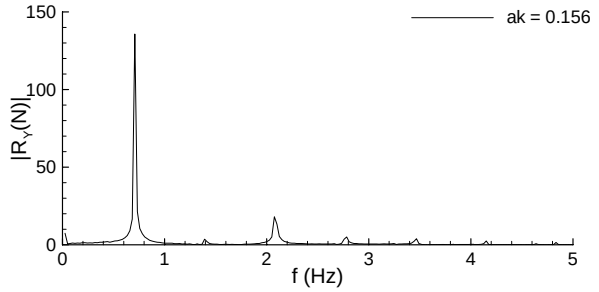

Figure 21: Amplitude function of the side force R_Y for the large amplitude waves.

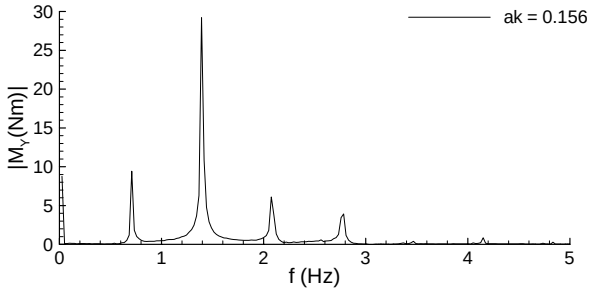

Figure 22: Amplitude function of the pitch moment M_Y for the large amplitude waves.

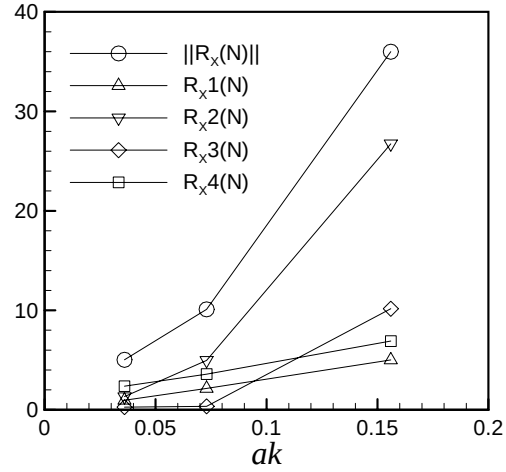

Figure 23 *a*: Amplitude of the axial force R_X versus the wave slope: total and first four harmonics.

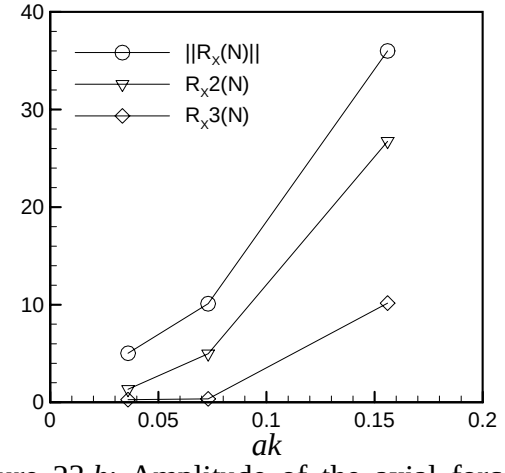

Figure 23 *b*: Amplitude of the axial force R_X versus the wave slope: total and 2nd and 3rd harmonic.

In figures 23 (*a, b, c*) the amplitude of the axial force $||R_X||$ defined by (1) is plotted together with the amplitudes of its first four harmonics (R_X1, R_X2, R_X3, R_X4) versus the wave slope. It is interesting to notice that the trend of the total amplitude is determined by the 2nd and 3rd harmonic, while the 4th

harmonic, which is dominant for the small amplitude waves, do not increase significantly with *ak*. Other remarkable feature is the linear increase of the fundamental R_X1 with the wave slope, as shown in figure 23 *c*.

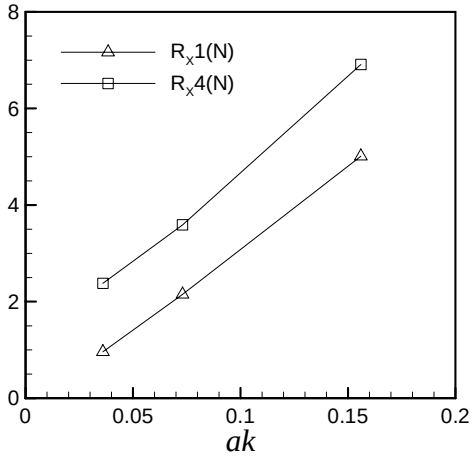

Figure 23 c: Amplitude of the axial force RX versus the wave slope: 1st and 4th harmonics.

In figure 24 the amplitude of the pitch moment $||M_Y||$ defined by (1) is plotted together with the amplitudes of its first three harmonics (M_Y1, M_Y2, M_Y3) versus the wave slope, while in figure 25 the amplitudes of the side force $||R_Y||$ and yaw moment $||M_Z||$ are plotted as a function of the wave slope. The yaw moment show a linear trend up to $ak = 0.073$, whereas it saturates for $ak = 0.156$. The three points related to the side force amplitude, seems to be aligned each other, but the line passing through them does not cross the origin, so that the trend with *ak* is nonlinear.

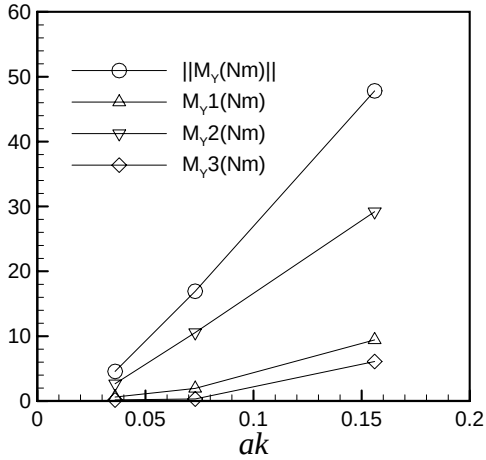

Figure 24: Amplitude of the pitch moment MY versus the wave slope: total and first three harmonics.

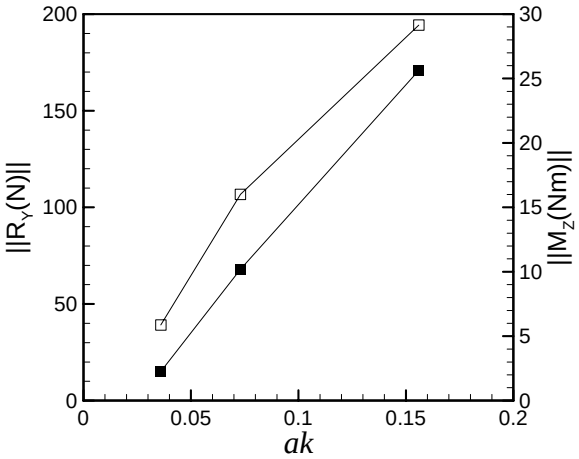

Figure 25: Amplitude of the side force RY (filled symbols) and yaw moment MZ (open symbols) versus the wave slope.

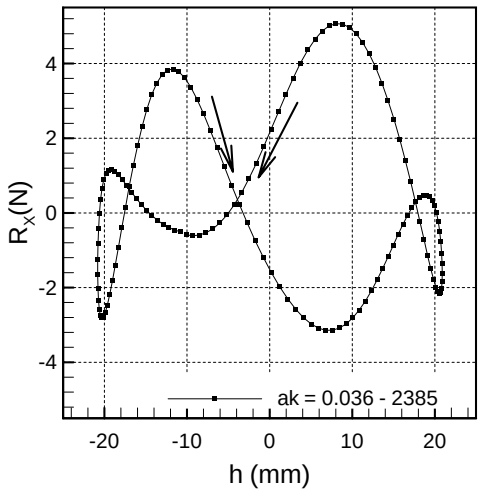

Figure 26: Combined plot of the axial force R_X versus the wave height (small amplitude waves).

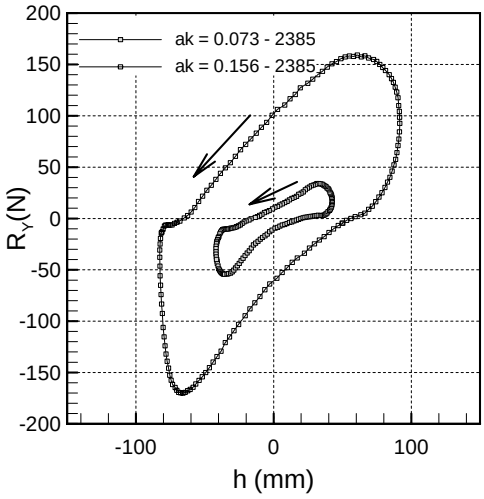

Figure 27: Combined plot of the side force RY versus the wave height.

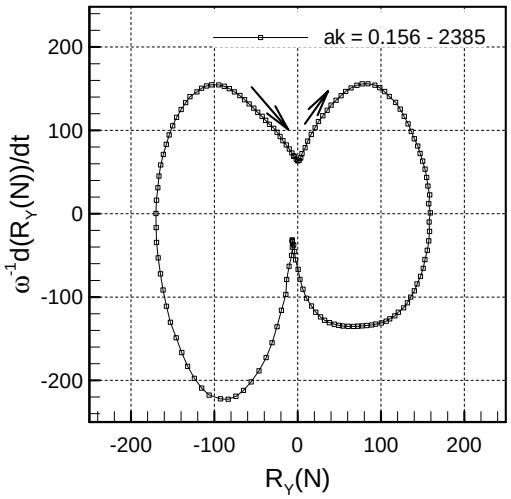

Figure 28: Phase diagram of the side force RY for the high amplitude waves.

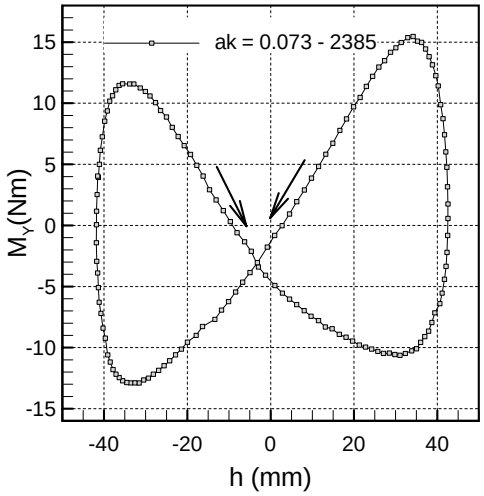

Figure 29: Combined plot of the pitch moment MY versus the wave height.

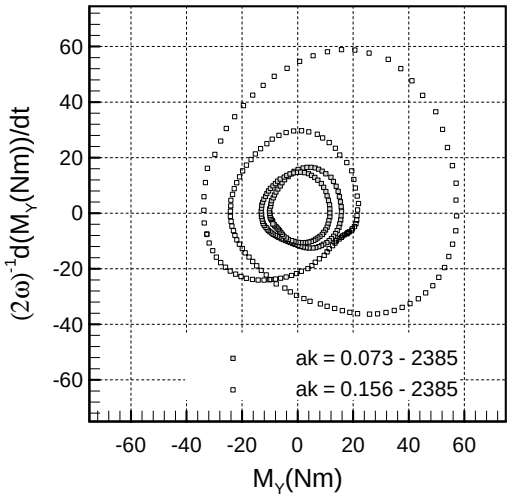

Figure 30: Phase diagram of the pitch moment MY for the high and medium amplitude waves.

The plot in figure 26 shows the four cycles of the axial force during one cycle of the wave height, while the plot in figure 27 confirms that the side force undergoes just one cycle each wave height cycle. On the other hand, the side force phase diagram in figure 28 shows a very peculiar trend, being close to the formation of a second cycle, which would indicate the presence of the 2nd harmonic. Different trend is shown by the pitch moment. The plot in figure 29 shows the presence of a "8-shaped" cycle each wave height cycle, as previously indicated by the preeminence of the 2nd harmonic in the amplitude function in figure 22 and confirmed by the phase diagram in figure 30.
Both axial force and pitch moment are almost zero for h = 0, while the side force cross the zero line close to the maximum and the minimum of the exciting wave.

3.2 ONR Tumblehome results (INSEAN model 2498)

As for the DTMB 5415, the heave motion well follows the wave height for all three cases and the roll motion shows no evidence of nonlinearities. In figure 31 the heave amplitude $||Z_G||$ is shown as a function of the wave height amplitude ||h|| together with the roll amplitude $||\phi°||$ versus the nominal wave slope *ak*. Both the heave amplitude and the roll motion show a linear growth with wave height and wave slope respectively.

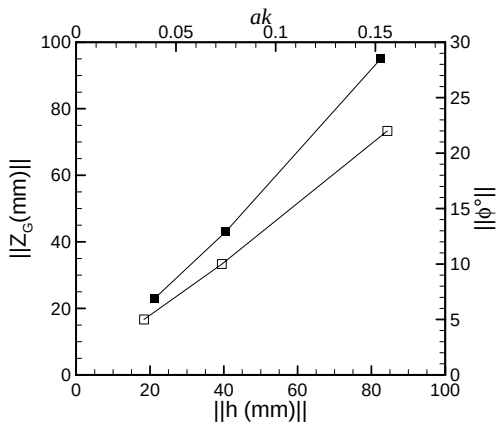

Figure 31: Heave amplitude ||ZG|| vs. wave height amplitude ||h|| (filled symbols) and roll amplitude || °|| (open symbols) vs. nominal wave slope *ak*.

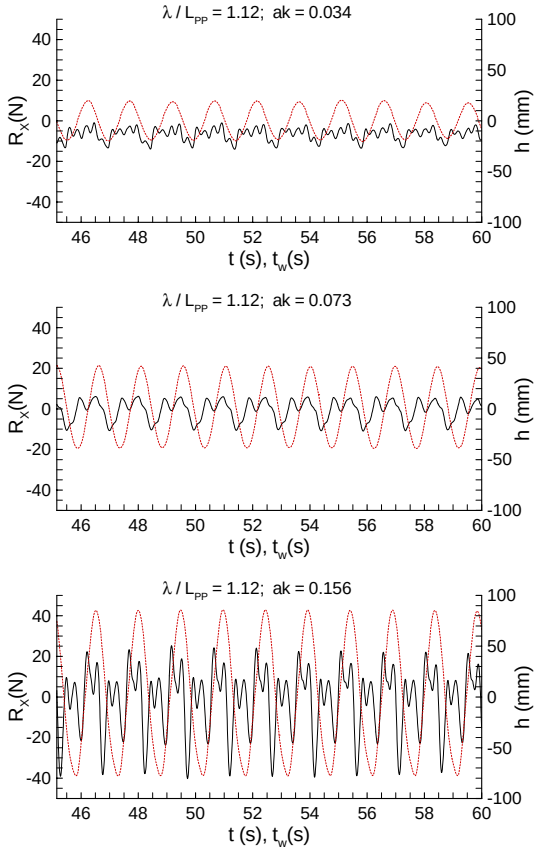

Figure 32: Time histories of the axial force RX (solid lines) superimposed to the time histories of the wave height (dashed lines)

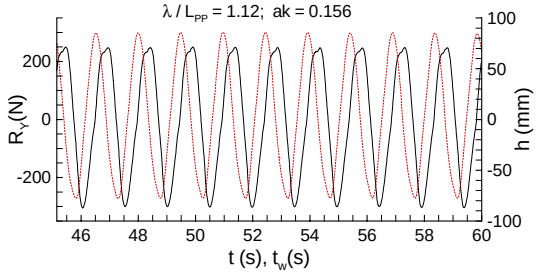

Figure 33: Time histories of the side force RY for large amplitude waves (solid line) superimposed to the time histories of the wave height (dashed line)

As for the DTMB 5415, nonlinear behavior is shown by the axial force R_X and pitch moment M_Y. Differently, the yaw moment M_Z shows a peculiar shape in the time history, especially for the highest wave slope, while the side force R_Y does not does not exhibit a particular behavior. As shown by figure 32, the time history of the axial force shows the presence of the 5th harmonic for the lowest *ak*, whereas for the higher wave slopes the 2nd harmonic starts to dominate (*ak* = 0.073). For the large wave amplitude case (*ak* = 0.156) the 5th harmonic is not visible by the time history, while the 4th harmonic becomes dominant. This behavior is confirmed by the Fourier analysis in figure 36.

The side force R_Y (figure 33) does not exhibit presence of higher harmonics as confirmed by the amplitude function in figure 37.

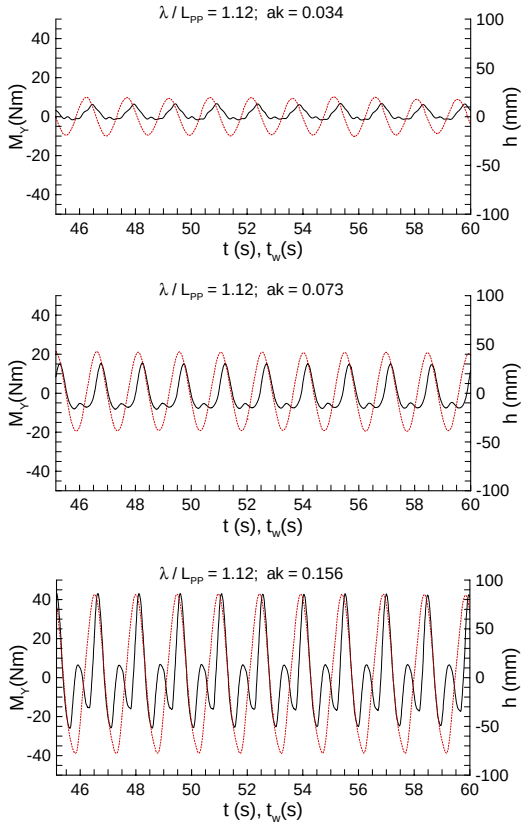

Figure 34: Time history of the pitch moment MY (solid lines) superimposed to the time histories of the wave elevation (dashed lines**)**

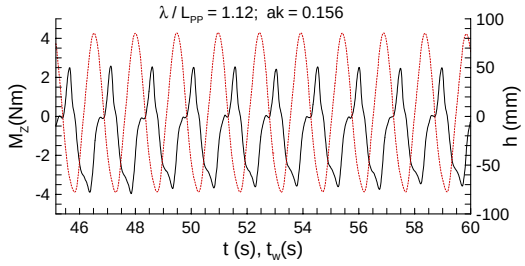

Figure 35: Time history of the yaw moment MZ for large amplitude waves (solid line) superimposed to the time histories of the wave elevation (dashed line)

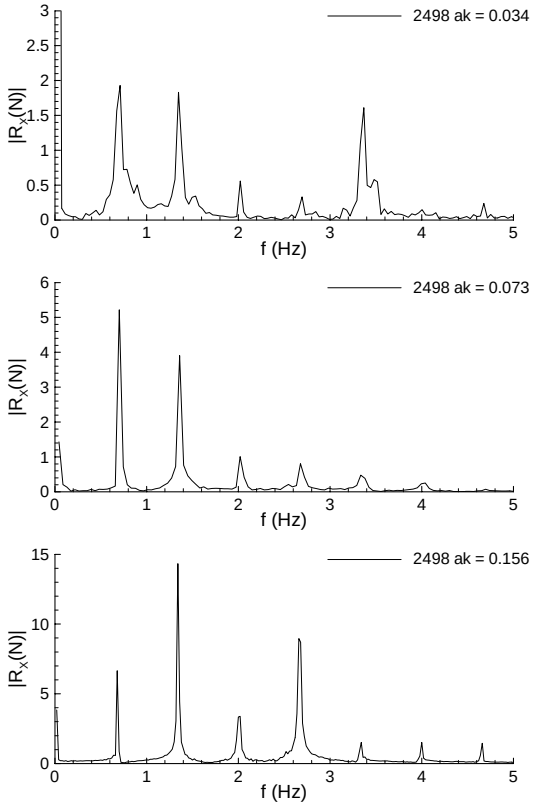

Figure 36: Amplitude function of the axial force RX for small, medium and large amplitude waves.

The pitch moment M_Y shows the presence of the 2nd harmonic even for the small wave amplitude case, although the preeminence of the fundamental is evident for the low and medium wave slopes. On the opposite, the 2nd harmonics dominates for ak = 0.156, as shown by figure 38, where the amplitude function for the three cases is represented.

The time history and the amplitude function of the yaw moment M_Z are shown in figures 35 and 39 for the large amplitude waves. Here, the 3rd harmonic is clearly visible, although it is much smaller than the fundamental component.

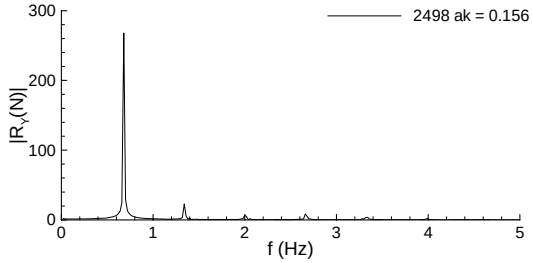

Figure 37: Amplitude function of the side force R_Y for the large amplitude waves.

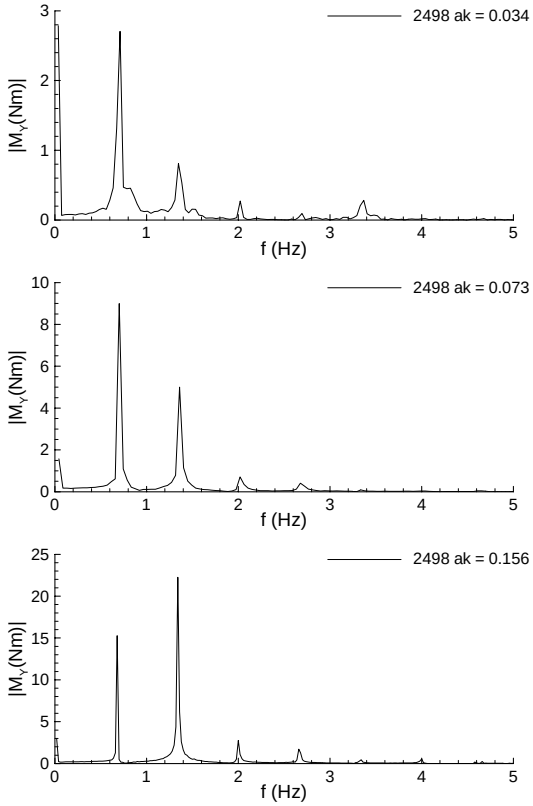

Figure 38: Amplitude function of the pitch moment MY for small, medium and large amplitude waves.

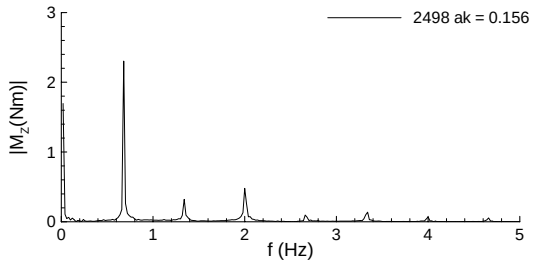

Figure 39: Amplitude function of the yaw moment MZ for the large amplitude waves.

The amplitude of the axial force and pitch moment is shown in figures 40 and 41 together with the amplitudes of their first four harmonics.

The side force amplitude grows linearly with the wave slope as shown in figure 42, where the yaw moment amplitude is also represented.

In figures 43 and 44 the combined plot of the pitch moment with the wave height and the phase diagrams of the pitch moment are shown

for the medium and large amplitude wave cases, showing respectively a “8-shaped” cycle and a double cycle, which confirm the development99 of the 2nd harmonic.

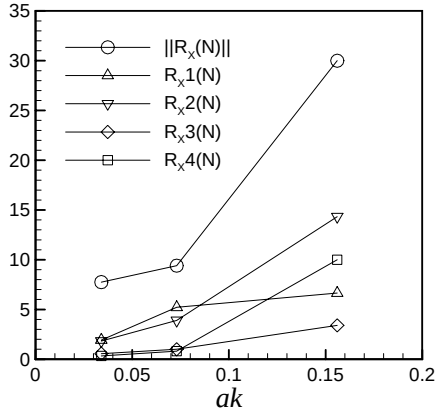

Figure 40: Amplitude of the axial force RX versus the wave slope: total and first four harmonics.

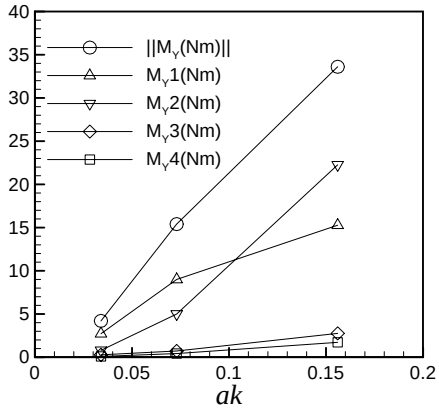

Figure 41: Amplitude of the pitch moment MY versus the wave slope: total and first four harmonics.

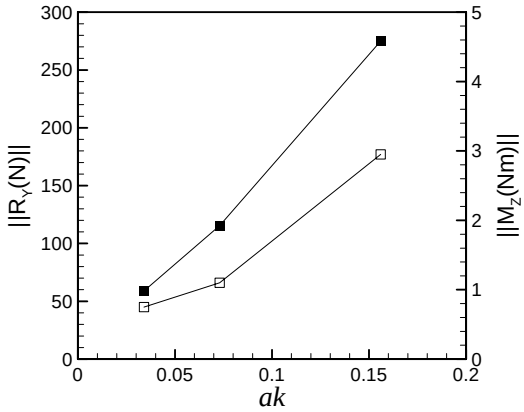

Figure 42: Amplitude of the side force RY (filled symbols) and yaw moment MZ (open symbols) versus the wave slope.

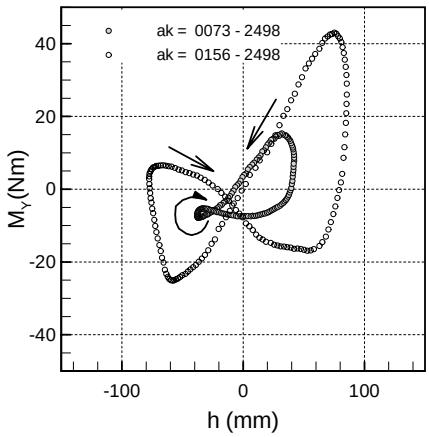

Figure 43: Combined plot of the pitch moment MY versus the wave height (medium and large amplitude waves).

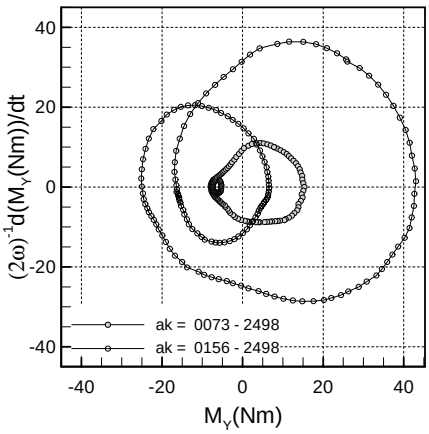

Figure 44: Phase diagram of the pitch moment MY for the high and medium amplitude waves.

3.3 Comparison of the results for DTMB 5415 and ONR Tumblehome

In order to correctly compare the results, they have been plotted using the measured wave slope (ak_M). In fact, we observed small variations on the wave height of the generated waves between the first tests on the DTMB 5415 and the second experimental campaign with the ONR Tumblehome. This could be ascribed to small differences on the water level in the basin or to small differences on the diffracted waves by the two models.

$$ak_M = \frac{2\pi \| h \|}{\lambda} \qquad (2)$$

In figure 45 the heave motion amplitude is represented as a function of the measured wave height amplitude. Both models show a linear trend with comparable amplitudes, although the 2385 saturates for the large amplitude wave case. Figure 46 shows the roll motion as a function of the measured wave slope. As for the heave, the tumblehome shows a very linear trend, while the 5415 saturates for the highest wave slope. Moreover, the roll motion of the tumblehome is quite smaller, probably due to the larger span of its bilge keels (Tables 1 and 2 and figures 3, 4 and 5).

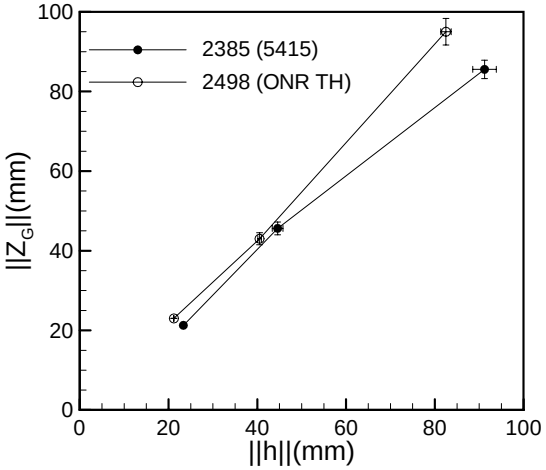

Figure 45: Heave motion amplitude versus the wave slope for both models with related PI bars.

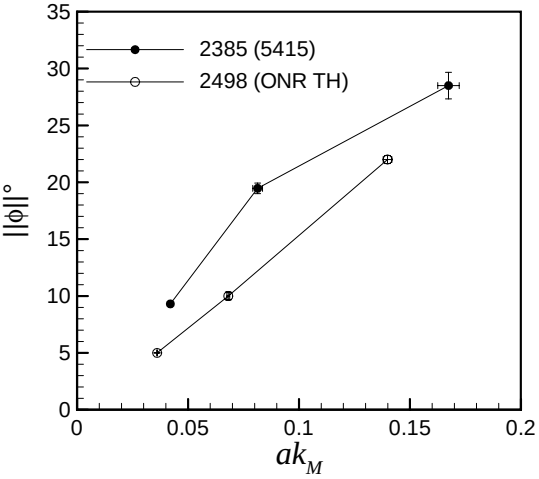

Figure 46: Roll motion amplitude versus the wave slope for both models with related PI bars.

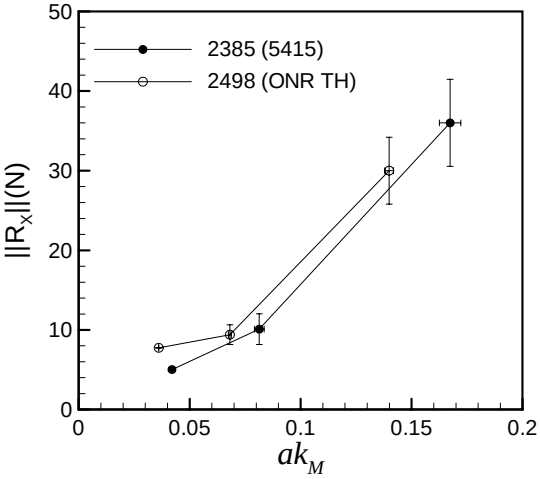

Figure 47: Axial force amplitude versus the wave slope for both models with related PI bars.

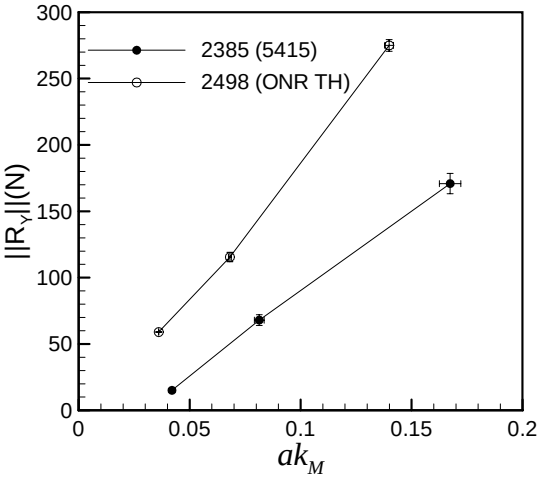

Figure 48: Side force amplitude versus the wave slope for both models with related PI bars.

The trends of the axial force are almost coincident with a small scatter for the small amplitude waves, probably due to a large measurement uncertainty (figure 47). In fact, for the small amplitude waves the reported values have been carried out based on a single test.

The side force amplitudes show large differences between the two models. The ONR Tumblehome experienced higher side forces with linear trend with respect to the wave

slope, while the DTMB 5415 undergoes lower side forces with non linear trend (figure 48).

The pitch moment is almost coincident, while the 5415 undergoes very high yaw moment, compared with the Tumblehome (figures 49 and 50). This can be related to the peculiar shape of the tumblehome, which does not present remarkable asymmetry between the aft body and fore body, with respect to the flare shaped 5415.

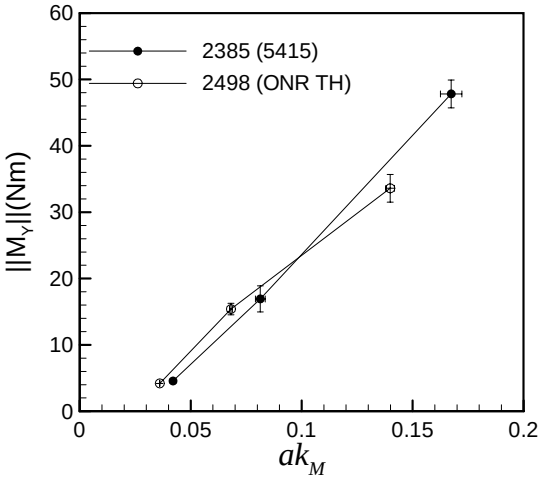

Figure 49: Pitch moment amplitude versus the wave slope for both models with related PI bars.

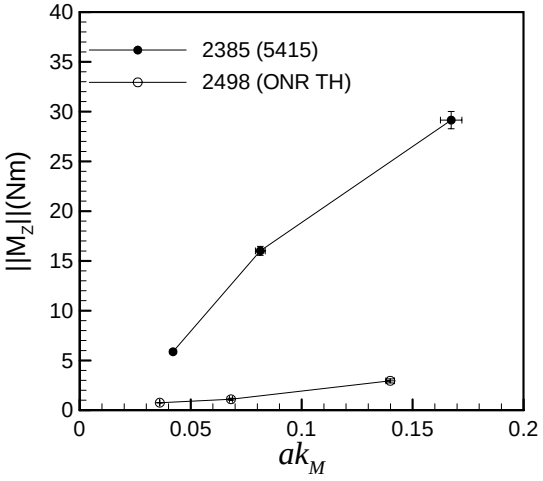

Figure 50: Yaw moment amplitude versus the wave slope for both models with related PI bars.

4. UNCERTAINTY ASSESSMENT

A detailed uncertainty assessment is still in progress. Here are presented the precision limit results (precision indexes), obtained by the repeated tests following the ITTC standards:

$$PI(x) = t_N \frac{\sigma(x)}{\sqrt{N}} \tag{3}$$

where x is the considered variable, σ is its standard deviation around the average on N repeated tests and t_N is the Student coefficient related to the 95% probability (Coleman and Steele, 1995).

The results are presented for the medium amplitude wave case (table 3) and the large amplitude wave case (table 4).

Table 3: precision index for DTMB 5415 (2385) and ONR Tumblehome (ak = 0.073)

	DTMB 5415		**ONR Tumblehome**	
Motion	Amplitude	**P1**	Amplitude	**P1**
Heave (Z_G)	45.6 mm	3.5%	44.5 mm	3.4%
Roll (ϕ)	19.5°	2.4%	10.4°	1.0%
Surge (R_X)	10.1 N	19.2%	9.4 N	13.1%
Sway (R_Y)	68.0 N	5.9%	115.5 N	3.1%
Pitch (M_Y)	16.9 Nm	11.6%	15.4 Nm	5.7%
Yaw (M_Z)	16.0 Nm	2.8%	1.1 Nm	9.1%

Table 4: precision index for DTMB 5415 (2385) and ONR Tumblehome (ak = 0.156)

	DTMB 5415		**ONR Tumblehome**	
Motion	Amplitude	**P1**	Amplitude	**P1**
Heave (Z_G)	85.6 mm	2.7%	91.0 mm	1.6%
Roll (ϕ)	28.5°	4.1%	21.5°	1.4%
Surge (R_X)	36.0 N	15.2%	30.0 N	14.0%
Sway (R_Y)	170.8 N	4.5%	275.0 N	1.6%
Pitch (M_Y)	47.8 Nm	4.4%	336.3 Nm	6.2%
Yaw (M_Z)	29.1 Nm	3.0%	3.0 Nm	6.8%

5. CONCLUDING REMARKS

Two different models of preliminary designs of surface combatants ca. 1980 (DTMB 5415) and present time (ONR Tumblehome) have been tested in regular beam seas in semicaptive conditions. The same scale has been adopted and the same facility and measurement systems have been used. The comparison of the results shows remarkable differences, especially for the roll amplitude, side forces and yaw moments. The use of captive tests instead of free running ones was dictated by the need of collecting results which can be used for validation of CFD codes. As a consequence, the results are not so realistic to allow ultimate conclusions in the frame of the comparison of dynamic stability of the two different ship forms. The roll motion amplitudes reported in figure 46, for example, don't describe the peak amplitude since they are obtained at constant frequency – nominally the small amplitude resonance frequency. This means they don't account for the different bending of the roll response curves as a consequence of the different righting arm curves. In addition, the restriction of sway introduces a non negligible disturbance in roll motion and yaw moment. It is also expected that the surge (axial) force can be influenced by the reflection of radiated waves from the walls. A detailed database for validation of theoretical and numerical models has been collected. The results are given in terms of time histories, Fourier analysis, combined plots and phase diagrams. In particular, the analysis of the results in terms of Fourier components can be very helpful for testing numerical codes. For all the presented results the precision limit has been determined on the basis of five repeated tests.

6. ACKNOWLEDGEMENTS

This work is sponsored by the Office of Naval Research contract N00014-04-1-0288 under the administration of Dr. Patrick Purtell.

Special thanks to F. Pistani, B. Jacob, M. Palini, R. Basti, F. Carta, R. Zagaglia, A. Ugolini, M. Sellini, L. Benedetti, M. Guerra, L. Brunacci for the fruitful discussion and their help in the preparation of the experimental set-ups and during the tests.

7. REFERENCES

Rojas P. L., Belenky V. L.,2005, "A Review of the 8th International Conference on the Stability of Ship and Ocean Vehicles (STAB 2003)" Marine Tech, Vol. 42, No. 1, January, pp. 21-30.

The Specialist Committee on Stability in Waves, 2005, "Final Report and Recommen-dations to the 24th ITTC" Proceedings of the 24th ITTC - Volume II, pp 369-408, Edinburgh, September

Wilson, R.V., Carrica, P.M., and Stern, F.,2006, "Unsteady RANS Method for Ship Motions with Application to Roll for a Surface Combatant," Computers & Fluids, Vol. 35, Issue 5, June, pp. 501-524.

Olivieri A., Campana, E.F., Francescutto A., and Stern F., Capsize Project Report: Part 1, IIHR Report (in preparation).

Coleman, H.W., Steele, 1888-1895, W.G. 1995 Engineering Application of Experimental Uncertainty Analysis. AIAA Journal, 33, 10..